ACS Sustainable Chemistry & Engineering

Research Article

Cite This: ACS Sustainable Chem. Eng. 2018, 6, 4194−4203

pubs.acs.org/journal/ascecg

Chemically Bonded Ni Cocatalyst onto the S Doped g-C_3N_4 Nanosheets and Their Synergistic Enhancement in H_2 Production under Sunlight Irradiation

Manh-Hiep Vu, M. Sakar, Chinh-Chien Nguyen, and Trong-On Do*

Department of Chemical Engineering, Laval University, Québec, Québec G1 V 0A6, Canada

Supporting Information

ABSTRACT: Nickel deposited S-doped carbon nitride (Ni−S:g-C_3N_4/Ni-SCN) nanosheets have been synthesized using calcination followed by a sulfidation process. X-ray photoelectron spectra revealed that the doped S atoms are successfully introduced into the 301 lattices of the host g-C_3N_4. XPS spectra indicated that the deposited Ni species are chemically bonded onto the host SCN nanosheets through sulfur bonds. The sunlight-driven photocatalytic hydrogen production efficiency of the synthesized Ni-SCN nanosheets is found to be 3628 μmol g^{-1} h^{-1}, which is around 1.5 folds higher than that of Pt-SCN that synthesized in the present study. The observed efficiency is attributed to the chemical bonding of Ni through S that largely favored the photocatalytic process in terms of charge-separation as well as self-catalytic reactions. The apparent quantum efficiency of the photocatalyst at 420 nm is estimated to be 17.2%, which is relatively one of the higher values reported in the literature. The photocatalytic recyclability results showed consistent hydrogen evolution efficiency over 4 cycles (8 h) that revealed the excellent stability of the photocatalyst. This work has demonstrated that the chemical bonding of cocatalyst onto the host photocatalyst is relatively an effective strategy as compared to the conventional deposition of cocatalyst by means of electrostatic or van der Waals forces.

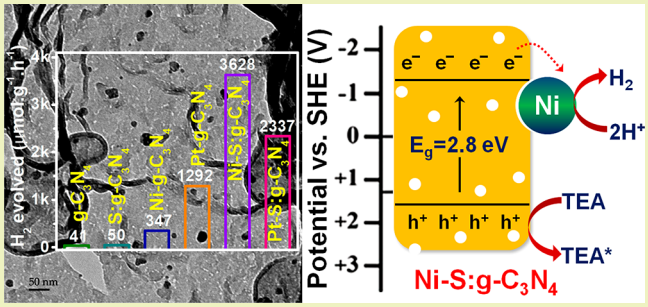

KEYWORDS: *Photocatalysis, Water splitting, Nanostructures, Band gap engineering, Nonmetal doping, Hydrogen evolution reaction, Carbon materials, Chemical synthesis*

INTRODUCTION

The increasing depletion of fossil fuels and the crisis for energy resources and the associated environmental issues have urged alternative routes toward the development of renewable energy sources through techniques such as photocatalysis, electrocatalysts, solar cells, rechargeable metal−air batteries, etc. to be found.[1−3] Of various techniques, photocatalysis has been realized to be one of the most promising approaches for the sustainable energy productions as it effectively converts the solar energy into chemical energy. Especially, since the last several decades, the photocatalytic H_2 evolution reaction (HER) through water splitting under solar energy has received tremendous attention because of its potential in concurrently dealing with the energy crisis and environmental problems.[4] In this direction, the noble metal sensitized photocatalysts have been found to be efficient for such effective water splitting applications.[5] However, the practical implementation of such a photocatalytic system is limited due to the cost of the noble metals. Therefore, the explorations of noble metal-free photocatalytic systems have gained significant interest. Among the various photocatalysts, the metal-free graphitic carbon nitride (g-C_3N_4/GCN), a nitrogen-rich carbon, is considered as a promising candidate for photocatalytic applications,[6,7] thanks to its promising features that include excellent stability, a narrow band gap energy ($E_g \approx 2.7$ eV),[8] straightforward preparation, and cost-effectiveness. However, the conventional bulk g-C_3N_4 exhibits limited photocatalytic activities due to a faster carrier recombination rate, originated by the weak $\pi-\pi$ conjugated stacked structure and low specific surface area. It has been reported that the recent strategies in the design of effective GCN-based photocatalysts comprise mainly the preparation of nanoscale GCN,[9−11] bandgap tailoring through doping,[12−17] molecular-modification, and the combination of GCN-based semiconductor composites.[4,18,19] Accordingly, the current and future developments in the field of g-C_3N_4 involve increasing their efficiency in terms of quantum efficiency yield (QEY) and solar-to-hydrogen (STH) conversion.[20] To achieve the former, g-C_3N_4 has been modified for their size and morphological designs and integrated with various types of materials to produce g-C_3N_4 hybrids and nanocomposites as to essentially increase their surface area and reduce the electron−hole recombination process. Similarly, to achieve the latter, g-C_3N_4 has been modified for their optical properties through making their hybrids with visible-light driven semiconductors

Received: December 5, 2017
Revised: January 18, 2018
Published: February 8, 2018

DOI: 10.1021/acssuschemeng.7b04598
ACS Sustainable Chem. Eng. 2018, 6, 4194−4203

(~600 nm), plasmonic nanomaterials, and doping with metals and nonmetals to suitably engineer their band gap to absorb full-sunlight energy (UV−vis−NIR).[20]

In particular, enormous attention has been devoted to the fabrication of nanosheets of GCN because of their thin-layered structure and large specific surface area, which could mainly overcome the existing limitations such as low surface area and poor stacking of the polymeric layers of GCN. Therefore, it is necessary to find appropriate methods for separating those bundles of layers into thin layers. Niu et al.[21] employed a conventional thermal-exfoliation of dicyandiamide-delivered bulk GCN to obtain the GCN-nanosheets with a high surface area of 306 m^2/g. However, the band gap of nanosheets was increased to 2.97 eV due to a decreased size, and it is known that the extended band gap energy may decrease the visible light absorption ability. On the other hand, the tunable band gap in GCN can be achieved by doping with foreign elements.[22−24] Especially, the band gap of the bulk GCN could be reduced by anion doping via three main strategies: (i) formation of localized states in the band gap structure, (ii) elevation of the valence band, and (iii) lowering of the conduction band.[25,26] It is known that the valence band (VB) of g-C_3N_4 is composed of a N 2p state, while the conduction band (CB) is composed of the hybridized N 2p and C 2p states. Therefore, the site-dependent substitution of elements helps with tuning the VB and CB edge positions. Especially, the doping of nonmetals such as S increases the visible light absorption efficiency of g-C_3N_4, due to the generation of localized energy levels in the band structure of the system.[25] In addition, it is reported that doping of nonmetals with low electronegativity relatively elevates the VB maximum.[27,28] The density functional theory (DFT) calculations also revealed that the band gap energy of g-C_3N_4 can be reduced by doping it with nonmetals such as S and P.[28] It is also concluded from the results that the nonmetal doping facilitates the photocatalytic activity of g-C_3N_4 by (i) increasing the visible light absorption, (ii) modifying their carrier mobility, and (iii) efficiently separating the electron−hole pairs in the system.[28] In this context, our strategy is to achieve the tunable band gap energy through S doping and to increase the surface area through the separation of the layers.

On the other hand, in the photocatalytic perspective, the integration of cocatalyst onto the host photocatalysts can effectively enhance their photocatalytic activities by means of charge-separation, transportation, and self-catalytic properties. Conventionally, the cocatalysts are often found to be noble metals such as Pt, Pd, etc.[23,24] However, the rarity and cost of these noble metals limit their practical applications in the scale up production of such noble-metal deposited photocatalysts. Therefore, the development of non-noble metal based cocatalyst with enhanced properties is a great challenge. Among the known non-noble metal cocatalysts, Ni has been realized to be one of the stable, active, and cost-effective cocatalysts toward HER and CO_2 reduction.[29,30] In particular, Ni has been reported as an ideal cocatalyst for sulfur-based photocatalysts such as CdS, $Cd_{1-x}Zn_xS$, and $ZnIn_2S_4$.[31−34] It is reported that the deposition of Ni^{2+} onto the g-C_3N_4 facilitates an efficient photochemical proton reduction and thereby enhances the H_2 production.[35] This is essentially due to the trapping of electrons in Ni that effortlessly reduce H^+ ions into H_2 as given in eq 1.[36]

$$Ni/2H^+ + 2e^- \rightarrow Ni + H_2 \quad (1)$$

However, the key issue in the above process is the conversion of Ni^{2+} ions to Ni^0, which considerably reduces the long-term proton reduction. Motivated by this issue, herein we have attempted a strategy to deposit Ni onto the g-C_3N_4 through S bonding and studied for their sunlight-driven photocatalytic properties toward H_2 production. This strategy of integrating the Ni cocatalyst by means of chemical bonding onto the host g-C_3N_4 nanosheets essentially facilitates a synergistic enhancement in the photocatalyst system as compared to the conventional cocatalyst integrated photocatalysts through electrostatic or van der Waals forces.

EXPERIMENTAL SECTION

Materials. Dicyandiamide, nickel ammonium sulfate, chloroplatinic acid hexahydrate, H_2S gas (5% H_2S; 95% N_2), ethanol, and distilled water were purchased from the commercial sources and used without further purification.

Synthesis of S-Doped g-C_3N_4. Graphitic carbon nitride was prepared by slightly modifying the method reported in the literature.[31] Briefly, 30 g of dicyandiamide precursor was calcined in a muffle furnace at 600 °C for 270 min with a heating rate at 2 °C/min. After cooling to ambient temperature, the as-prepared g-C_3N_4 sample (denoted as GCN) was washed with distilled water and ethanol several times and dried at 60 °C overnight. In the next step, the dried sample was further treated under H_2S gas that purged at an optimized flow rate of 4 L/h at 450 °C for 2 h (the H_2S treated g-C_3N_4 is denoted as SCN). Then, Ni was photodeposited onto the prepared pristine and S-doped GCN, and further, Pt-deposited carbon nitride samples were also prepared toward their comparison studies.

Photodeposition of Ni onto SCN. Typically, 50 mg of photocatalyst was dispersed in 100 mL of aqueous solution of 10% triethanolamine, which acts as a sacrificial reagent. Then, the mixture was purged with nitrogen for 30 min to remove dissolved oxygen. After that, an optimized amount of 2 wt % of Ni precursor was added to the above dispersion and stirred well for 30 min, and then solution-dispersion was irradiated with the simulated solar light. The change of solution color from white to grayish indicated the Ni disposition onto the samples as shown in Figure S1, given in the Supporting Information. Finally, the Ni-supported SCN was washed with distilled water and ethanol before testing photocatalytic activity and further characterizations. This process was repeated with Pt-precursor as to prepare the Pt-deposited samples.

Characterizations. Transmission electron microscopy (TEM) images of the samples were obtained on a JEOL JEM 1230 operated at 120 kV. Powder X-ray diffraction (XRD) patterns of the samples were obtained on a Bruker SMART APEXII X-ray diffractometer equipped with a Cu Kα radiation source (λ = 1.5418 Å). X-ray photoelectron spectroscopy (XPS) measurements carried out in an ion-pumped chamber (evacuated to 10^{-9} Torr) of a photoelectron spectrometer (Kratos Axis-Ultra) equipped with a focused X-ray source (Al Kα, $h\nu$ = 1486.6 eV). The UV−vis absorption spectra were recorded on a Cary 300 Bio UV−vis spectrophotometer. Fourier transform infrared (FTIR) spectra were measured with an FTS 45 infrared spectrophotometer with the KBr pellet technique. The photocurrent measurements were carried out in a conventional three electrodes station (Autolab PGSTAT204).

Photocatalytic Studies. In a typical photocatalytic experiment, first, an optimized amount of 50 mg of the photocatalyst was dispersed in a solution containing 90 mL of water and 10 mL of a sacrificial agent triethanolamine (TEA), which was taken in a reactor cell. Then, the reactor cell was illuminated using a solar simulator 150 W Xe lamp for 2 h, and the evolved hydrogen was measured using GC. This procedure was repeated for four cycles, where the residual hydrogen was removed by purging the nitrogen gas for 30 min before starting every new cycle. The amount of H_2 gas generated was determined using a gas chromatograph (GC) equipped with a thermal conductivity detector (TCD) and N_2 as the carrier gas.

DOI: 10.1021/acssuschemeng.7b04598
ACS Sustainable Chem. Eng. 2018, 6, 4194−4203

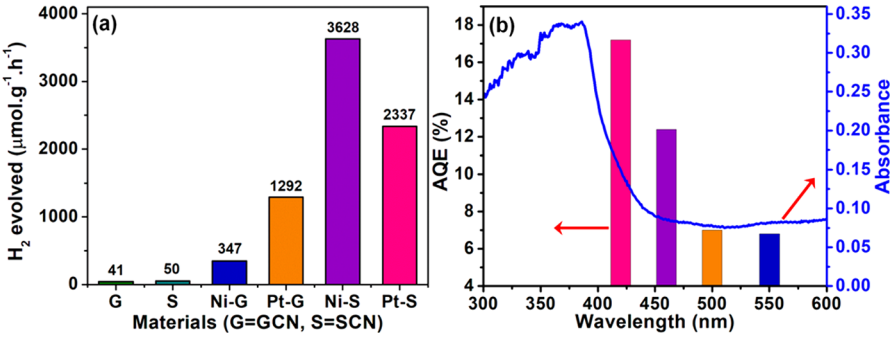

Figure 1. (A) Photocatalytic hydrogen evolution over various samples under solar light; (B) AQE values of H_2 production over the Ni-SCN sample under various monochromatic light irradiations given with respect to its absorption spectrum.

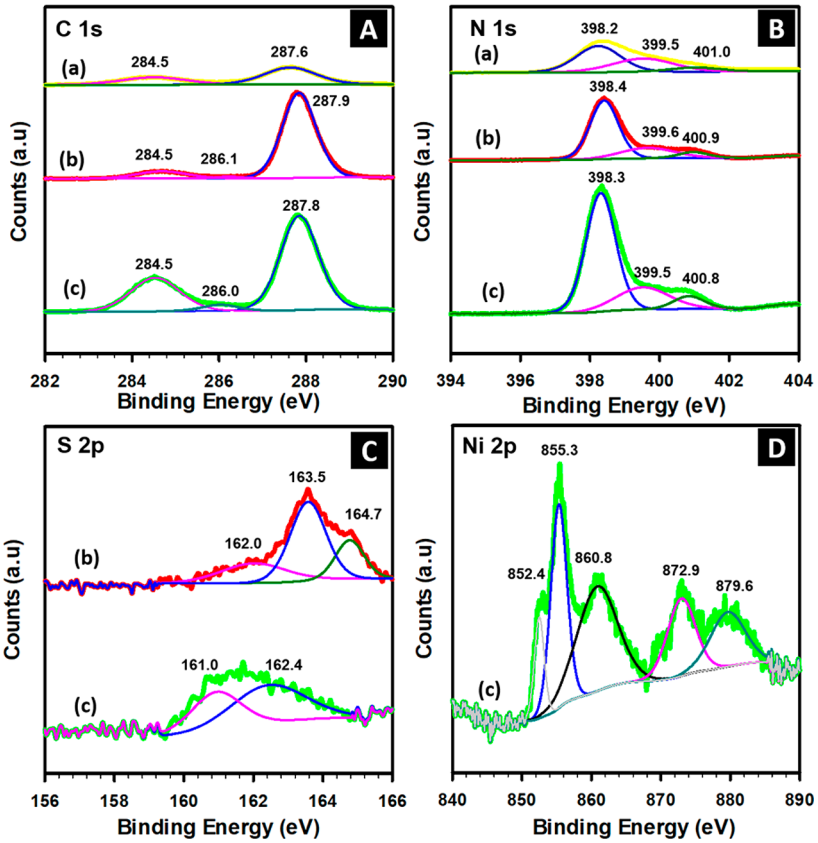

Figure 2. XPS spectra of (A) C 1s, (B) N 1s, (C) S 2p, and (D) Ni 2p. Inset figures (a) GCN, (b) SCN, and (c) Ni-SCN.

The apparent quantum efficiency (AQE) of the prepared sample was calculated according to the following equation;

$$\text{AQE}(\%) = [\text{number of reacted electrons or holes}] / [\text{number of incident photons}] \times 100$$
$$= [2 \times \text{number of } H_2 \text{ molecules evolved}] / [\text{number of incident photons}] \times 100$$

Photoelectrochemical Measurements. The working electrodes were prepared as follows: 5 mg of photocatalysts was dispersed in 2.5 mL of ethanol and 2.5 mL of isopropanol to make the slurry of the materials. Then, the slurry was coated onto a 1 cm × 1 cm F-doped SnO_2-coated (FTO) glass electrode by spin coating technique. Next, the as-prepared electrodes were dried overnight and calcined at 350 °C in a nitrogen gas flow. Transient photocurrent response was performed on an electrochemical workstation (Autolab PGSTAT204) based on a standard three-electrode system using the as-prepared electrodes as the working electrodes. A Pt wire and Ag/AgCl was used as the counter electrode and reference electrode, respectively. The photocurrent was measured under solar light irradiation (150 W xenon lamp) with 10 s light on−off cycles. For the electrochemical impedance (Nyquist plots) measurements, the perturbation-signal was set to be 10 mV and the frequency range was from 0.1 MHz to 0.1 Hz.

RESULTS AND DISCUSSION

Figure 1A shows the simulated-sunlight driven photocatalytic hydrogen production of the Ni and Pt deposited GCN and SCN samples. The obtained results showed that the Ni-SCN exhibited the highest hydrogen production efficiency as compared to Pt-SCN at the same concentration. In contrast, the Ni-GCN showed decreased photocatalytic efficiency as compared to Pt-GCN. This observation clearly indicates that the S doping in g-C_3N_4 readily facilitates the integration of Ni than that of Pt and the favors enhanced photocatalytic

DOI: 10.1021/acssuschemeng.7b04598
ACS Sustainable Chem. Eng. 2018, 6, 4194−4203

reactions. This enhancement could be attributed to integration mechanics of Ni onto the SCN. In addition to this, the quantum efficiency (QE) of the Ni-SCN was calculated and found to be 17.2% at 420 nm (Figure 1B), which is relatively one of the higher values in the literature as listed in Table S1-given as the Supporting Information. The calculated AQE values of Ni-SCN nanosheets at different wavelengths with respect to their absorption spectrum are shown in Figure 1B.

In order to gain insights into the observed photocatalytic efficiency, the samples were further analyzed in detail. Accordingly, the high-resolution XPS spectra of C, N, S, and Ni in the respective pristine g-C_3N_4, SCN, and Ni-SCN samples are obtained and displayed in Figure 2A–D, respectively. As shown in the C 1s spectra of GCN (Figure 2A), the deconvoluted peak centered at 284.5 and 287.6 eV could be attributed to sp^3-bonded carbon in C–C and N–C=N, correspondingly. However, the XPS peak of N–C=N is found to be a positive shift to higher binding energy at 287.9 and 287.8 eV in SCN and Ni-SCN samples. This may be due to that factor that, during H_2S treatment at high temperature, some of the C atoms in tri-s-triazine units leached and leading to carbon vacancies in the SCN, which is also further confirmed by elemental analysis as provided in Table S2 in the Supporting Information. Moreover, the observed increase in the intensities of the C 1s spectra of both SCN and Ni-SCN demonstrated that C atoms neighboring carbon vacancies are reduced electron density than those ones on the normal sites,[37] leading to a shifted peak to higher binding energy. The existence of a hump-like peak at 286.1 and 286.0 eV in XPS spectrum of SCN and Ni-SCN, respectively, can be assigned to C–O bonding,[38] which may be originated from the absorbed oxygen on the surface.

The XPS spectra of N in pristine g-C_3N_4, SCN, and Ni-SCN are shown in Figure 2B. The N 1s spectrum is found to be similar for all of the samples, except the variation in the profile of the peaks. The deconvoluted peaks located at ~398.2 eV can be ascribed to the sp^2-bonded nitrogen in C–N=C groups while the peaks at ~399.5 eV correspond to the nitrogen in the tertiary group (N-$(C)_3$). In addition, the amino-functional groups with a hydrogen atom C-NH can be attributed to the weak peaks at ~401.0 eV. The observed peak of S 2p for SCN at 164.5 eV is due to the lattice S in the host g-C_3N_4 (Figure 3C). Similarly, the peaks located at 162.0 and 163.5 eV correspond to C–S bonds in SCN. Importantly, these observed binding energies indicate the −2 oxidation state of S atoms in SCN. On the other hand, these characteristic peaks are found to be shifted toward lower binding energy by around 1.0 eV in the case of Ni-SCN. This essentially indicates that the interaction of Ni with SCN is not through physisorption, but it could be due to the chemisorptions, where it reveals that Ni is chemically bonded onto the SCN rather than the through electrostatic or van der Waals interactions. Further, the peak corresponding to the lattice S (164.7 eV) is completely suppressed as it is largely dominated by Ni through their chemical bonding with S in the SCN. Moreover, it should be noted that the S atoms replace the N atoms and make bond with C atoms in SCN system, while in Ni-SCN, the S atoms also make bonding with Ni atoms. Therefore, the chemical environment of the S species is different in the SCN as compared to their chemical environment in Ni-SCN. These changes in the chemical environment of S atoms lead to significant modifications in both the binding energy and profile of XPS peaks of S species. It is also noteworthy that the physisorption such as electrostatic interaction will lead to only a slight shift in the binding energy of the species as the interaction occurs through the electrical charges, while the chemisorptions make significant changes in the binding energy as the species are chemically bonded. Accordingly, during the photodeposition process, the adsorbed Ni^{2+} ions on the SCN sample readily bind with S^{2-} species in the host SCN, thereby it establishes a strong chemical bonding between the deposited Ni and the host SCN, through the Ni–S–C-N bond formation in the system.

The XPS spectrum of Ni 2p is displayed in Figure 2D, where the deconvoluted peak at 852.4 eV indicates the zero oxidation state (metallic Ni) of Ni, while the other two peaks at 855.3 and 860.8 eV can be assigned to Ni^{2+} that are due to the formation of Ni–S bonds. Sergey et al.[39] reported that the sulfur tends to donate its electron to the $\pi-\pi$ conjugation system to form p_x and p_y orbitals, while in some cases a partial back-donation of electrons to the S p_z orbital also takes place. It is therefore the metallic nickel with an electron pair occupied in the s orbital that become electron donors which can easily donate electrons to S p_z orbital to form Ni–S bonds. Such chemical bonding will essentially lead to an increase in the electron density in S atoms along with increasing electron density in C atoms, which leads to a significant shift toward the lower binding energy in the XPS spectra of Ni-SCN. These results suggest that the Ni is chemically bonded onto the S doped g-C_3N_4, which effectively drives the charge carriers and enhances the photocatalytic reactions.

Figure 3 shows the XRD pattern of the synthesized pristine g-C_3N_4, SCN, and Ni-SCN samples. The obtained XRD patterns indicate the crystalline phase of g-C_3N_4 without any secondary or impurity phase (JCPDS no. 87-1526). The two respective peaks centered at 13.1° (100) and ~27.8° (002) are attributed to the in-plane structural packing of tri-s-triazine motifs and repeated interplanar stacking of conjugated aromatic systems corresponding to the stacking distance of 0.682 and 0.326 nm, respectively.[40] The observed slight shift in the XRD pattern of bare g-C_3N_4 with respect to the standard peaks may be due to the reduced size (layer thickness) of g-C_3N_4 layers, while the standard patterns conventionally represent the bulk materials. Similarly, it should be noted that the profile of the peak corresponding to the (100) plane is found to be significantly modified for SCN and Ni-SCN as compared to GCN, which could be attributed to the reduced length of the interlayer periodicity and the larger distance between carbon nitride nanosheets, which occurred possibly due to the lattice-occupation of S atoms in the host g-C_3N_4. Similarly, a visible shift can be observed for SCN and Ni-SCN with respect to

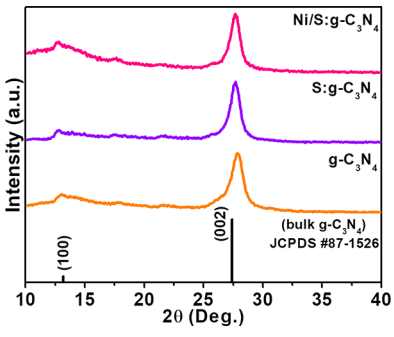

Figure 3. X-ray diffraction patterns of the synthesized samples.

DOI: 10.1021/acssuschemeng.7b04598
ACS Sustainable Chem. Eng. 2018, 6, 4194–4203

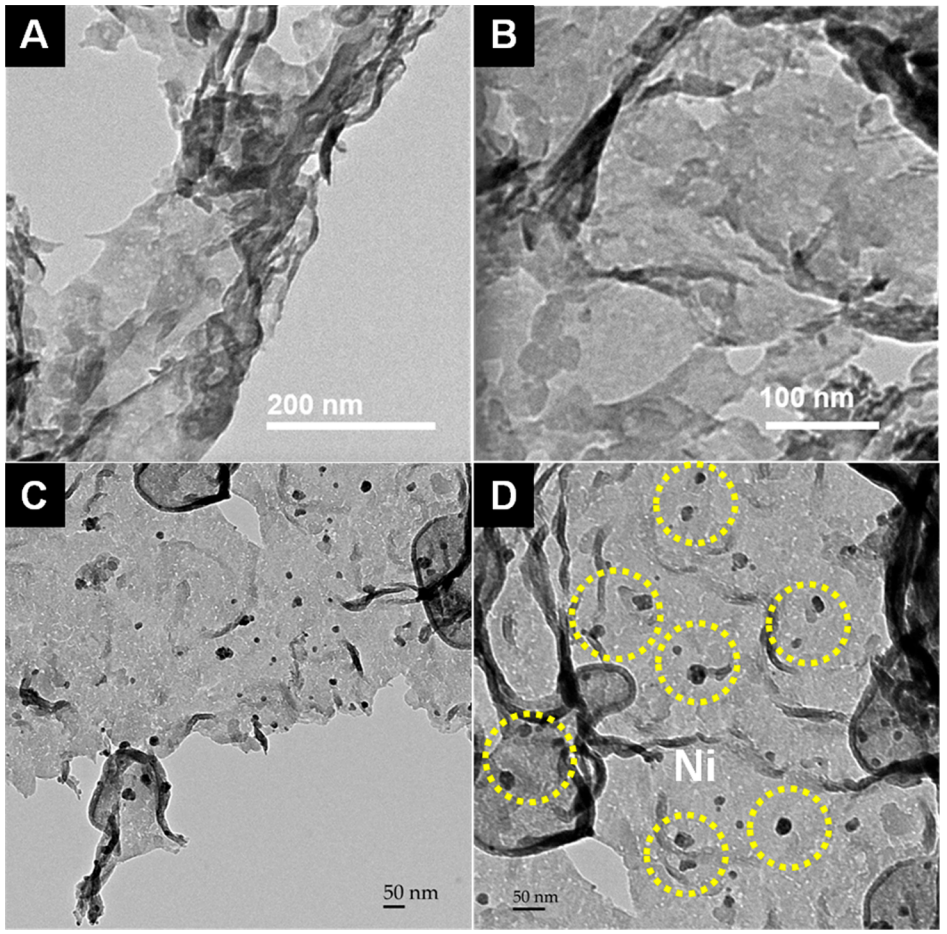

Figure 4. (A and B) TEM images of SCN and (C and D) TEM images of Ni-SCN.

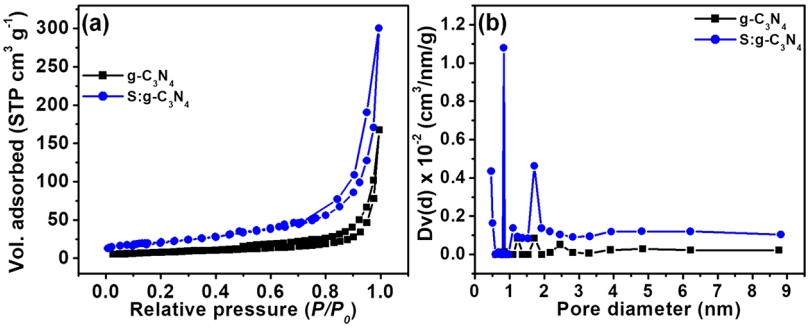

Figure 5. (a) Nitrogen adsorption−desorption isotherms at 77 K and (b) pore-size distribution.

GCN, which could be attributed to the doping-induced modification in the lattices and structure of the g-C_3N_4 layers.

The transmission electron microscopy (TEM) images of SCN and Ni-SCN, as given in Figure 4A−D, show their typical 2D nanosheet-like structures with a corrugated thickness of around 30 nm. It can be seen that the surface of SCN is likely found to be porous with nanosized holes that may be formed due to the high-temperature formation of SCN at 600 °C. It should be noted that these nanoholes and distorted atomic arrangement essentially serve as rich-active sites and may lead to a significant enhancement in the charge transfer characteristics of the nanosheets and improvement in their photocatalytic activities. Figure 4C,D displays the TEM images of Ni-SCN, where the average size of the integrated Ni nanoparticles is measured to be 10 nm, and they are found to be highly dispersed on the surface of SCN, which might have possibly functioned as abundant reduction and self-catalytic sites over SCN surface.

The CNSH elemental analysis of the SCN sample is given in Table S2 (in the Supporting Information). The respective stoichiometric ratio of C/N and sulfur content is determined to be 0.56 and 0.6 at. %, suggesting that sulfur is successfully introduced into the host g-C_3N_4. Also, the off-stoichiometric C/N ratio suggested a number of carbon vacancies presented in the sample of SCN. The N_2 adsorption/desorption isotherm and pore-size distribution curves of the GCN and SCN are shown in Figure 5a,b, respectively. From the results, the specific surface area of GCN is calculated to be 26 m^2/g, which is increased to 85 m^2/g for SCN. This could be attributed to (i) the thermal exfoliation of GCN during H_2S treatment, which

DOI: 10.1021/acssuschemeng.7b04598
ACS Sustainable Chem. Eng. 2018, 6, 4194−4203

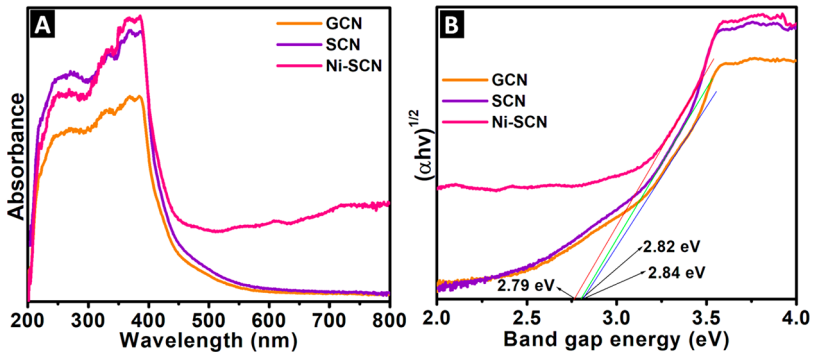

Figure 6. (A) UV−visible absorption spectra of GCN, SCN, and Ni-SCN; (B) estimation of band gap energy of GCN, SCN, and Ni-SCN.

reduced the thickness of GCN layers by separating the stacked layers along with the S doping, and (ii) the porous surface of SCN. These changes in the size and morphological parameters eventually resulted to the increased specific surface area of SCN.

The UV−vis absorption spectra of GCN, SCN, and Ni-SCN are presented in Figure 6A, and the band gap energies of the obtained materials were calculated using Tauc plot[41,42] and found to be 2.84, 2.81, and 2.79 eV for GCN, SCN, and Ni-SCN, respectively (Figure 6B). Both GCN and SCN showed a similar absorption profile with a strong absorption edge around 400 nm along with a slight absorption enhancement for SCN. By contrast, the absorption curve of Ni-SCN extended up to 800 nm as compared to GCN and SCN. It should be noted that the S-doping on GCN has not led to any "shift" in the absorption profile essentially because of the hardly altered band gap structure of SCN. This may be due to the amalgamated role of S doping and the carbon vacancy defects along with the reduced size of SCN layers. In general, while the S doping and defects tend to reduce the band gap energy of SCN, the reduced size of SCN layers tends to increase it. Therefore, the competition between the S doping induced defects and reduced size of SCN layers resulted to the relatively unmodified optical properties in SCN. Similarly, the absorption profile of Ni-SCN is also not largely altered except an extended absorption band edge in the range from 450 to 800 nm, which could be attributed to the chemical bonding of Ni onto the host SCN. It is discussed that the VB and CB of g-C_3N_4 are composed of N 2p states and hybridized N 2p-C 2p states, respectively. Accordingly, it is found that the doping of S atoms into the N site slightly modified their optical properties. Under such circumstances, the Ni, which is chemically bonded through the S atoms, creates localized electron trapping centers that influenced the optical properties of the material and led to an extended absorption up to 800 nm as akin to the plasmon-sensitized systems.

The FTIR analysis was performed in order to investigate the chemical bonding in GCN, SCN, and Ni-SCN nanostructures, and obtained spectra are shown in Figure 7. The FTIR skeletal structure of g-C_3N_4 is found to be unaltered due to S doping and Ni integration. However, the intensity of the peaks is decreased, which essentially represents the influence of S and Ni over the stretching of C−N bonds. Accordingly, the observed signals in the range from 1200 to 1650 cm^{-1} could be assigned to the stretching vibrations of heptazine heterocyclic ring (C_6N_7) units.[43,44] The peak that appeared at 810 cm^{-1} represents the characteristic breathing vibration of triazine units, which is due to the condensed-CN heterocycles.[45] The

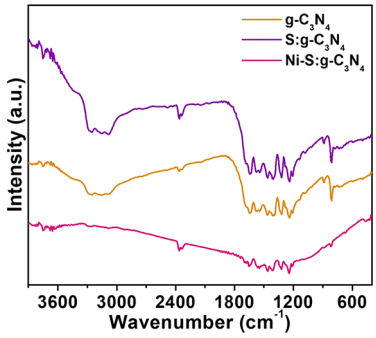

Figure 7. FTIR spectra of the synthesized materials.

peak at 885 cm^{-1} could be ascribed to the deformation of N−H bonds.[46] A band at 2380 cm^{-1} can be assigned to the adsorbed CO_2 on the surface of the samples. The bands in the range from around 2900 to 3500 cm^{-1} region can be ascribed to the adsorbed H_2O molecules and N−H vibration of the uncondensed amine groups[47] in the compositions. Interestingly, these bands are almost disappeared for Ni-SCN, which could be due to the S doping as it established a surface chemical bonding through the Ni−S−C-N formation. Overall, the absorbed decreased intensity in the FTIR spectrum of Ni-SCN with respect to GCN and SCN could be attributed to the S doping, Ni integration, and sized reduction induced changes in the chemical bonding in the functional groups of the g-C_3N_4 structure.

Figure 8A shows the amount of hydrogen generated over the Ni-SCN system with different Ni concentrations. It should be noted that the loading of Ni cocatalyst on SCN significantly enhances the photocatalytic activity toward H_2 evolution. Without cocatalyst, only around 50 μmol g^{-1} h^{-1} of hydrogen was evolved. Interestingly, at 1 wt % Ni-SCN, the production rate can be drastically increased to 3107 μmol g^{-1} h^{-1}. It was further observed that the increasing amount of Ni to 2 wt % led to production of the highest yield of 3628 μmol g^{-1} h^{-1} H_2 molecules. However, at the higher loading of Ni at 3 wt %, the H_2 production efficiency was relatively decreased to 2528 μmol g^{-1} h^{-1}. It may be due to the poor bonding of Ni onto the SCN and screening behavior of excess Ni on the surface of SCN, which eventually inhibited the ability of light absorption and subsequent charge separation and transportations. Also, the photocatalytic activities of S doped g-C_3N_4 and Pt integrated SCN with increasing concentrations were also obtained and the results are shown in Figure S2(a)-(b), respectively, in the Supporting Information. From the results, it was observed that the H_2 production is found to be 1437, 2337, and 1828 μmol

DOI: 10.1021/acssuschemeng.7b04598
ACS Sustainable Chem. Eng. 2018, 6, 4194−4203

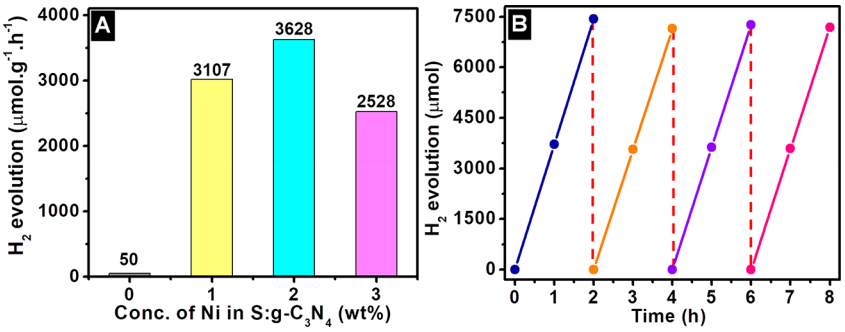

Figure 8. (A) Photocatalytic hydrogen evolution over Ni-SCN photocatalysts; (B) recyclable efficiency of Ni-SCN.

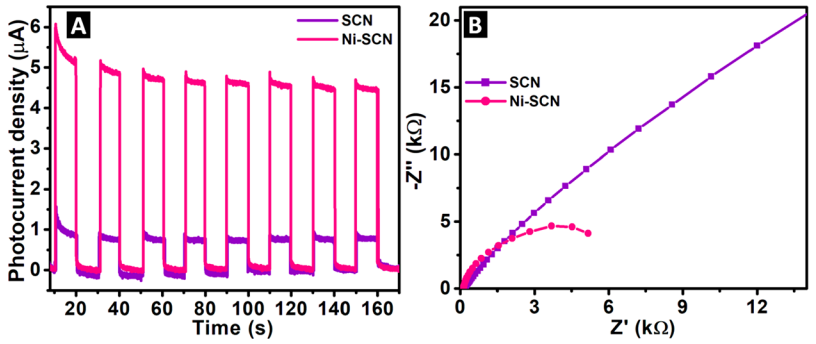

Figure 9. (A) Photocurrent response and (B) Nyquist plots for electrochemical impedance of SCN and Ni-SCN photocatalyst.

g^{-1} h^{-1} for 1, 2, and 3 wt % Pt-SCN, respectively. These results demonstrated that the Ni integration is exceptionally better than Pt-SCN, which is mainly because of the factor that S doping sufficiently modifies g-C_3N_4 as to facilitate the chemical bonding of Ni cocatalyst. Further, the recyclability of Ni-SCN photocatalyst was also evaluated and it exhibited an enhanced stability over four cycles (for 8 h) without any significant decrease in its activity (Figure 8B). Further, as mentioned in the introduction, Ni^{2+} could trap electrons for H_2 production, and the conversion from Ni^{2+} to Ni^0 would result in its decreased performance. Accordingly, the stability of Ni through the inhibition of Ni^{2+} to Ni^0 conversion due to Ni−S bonding is further verified using XPS technique by recording the Ni spectrum of recycled Ni-SCN along with its TEM image as shown in Figure S3(a)-(b) given in the Supporting Information. It suggests that chemically bonded Ni-SCN could be a promising photocatalyst for hydrogen evolution through water splitting process.

As to further validate the observed results, the photocurrent efficiencies and electrochemical impedance behavior of SCN and Ni-SCN are studied and the obtained results are displayed in Figure 9A,B, respectively. The photocurrent response of the samples was obtained via eight on−off cycles. It is clearly seen that the photocurrent density of Ni-SCN is increased nearly 5 times as compared to SCN, which demonstrates a significant improvement in the separation of photogenerated charge carriers.[35] Similarly, it can be observed from the Nyquist plots (Figure 9B) that the impedance of SCN is much higher than Ni-SCN, which suggests there is an enhanced charge transferring ability of Ni-SCN than that of SCN.[35] This further confirms the better charge transfer and decreased recombination possibilities in Ni-SCN, which is consistent with the photocurrent response of the sample. These observed enhancements could be attributed to the chemically bonded Ni-cocatalyst onto SCN that largely facilitates the photocurrent and improves the rapid migration of generated charge carriers to the surface.

Based on the above results, the photocatalytic efficiency of Ni-SCN can be explained as follows, and the schematic illustration of the mechanism is given in Figure 10A,B. The

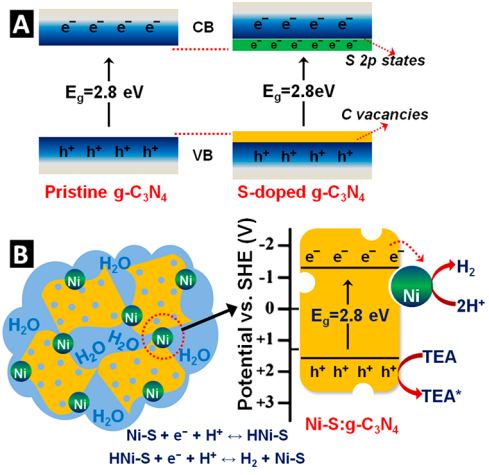

Figure 10. Illustration of (A) band gap formation and (B) photocatalytic hydrogen evolution mechanism of Ni-SCN photocatalyst under solar light.

mechanism of the observed efficacy could be attributed to two stages of the process: (i) enhanced charge separation and transportation and (ii) the self-catalytic behavior of chemically bonded Ni cocatalyst. Accordingly, the former could be attributed to the chemically bonded Ni−S induced modification in the band structure of g-C_3N_4,[25] where it forms new energy levels underneath the conduction of band (CB) as the energy states of S hybridized with C−N states, where it facilitates

DOI: 10.1021/acssuschemeng.7b04598
ACS Sustainable Chem. Eng. 2018, 6, 4194−4203

extended visible light absorption and rapid charge separation and transportations as shown in Figure 10A, which is evidenced from the XPS results, transient photocurrent response, and impedance results. Similarly, the latter mechanism, which is the self-catalytic behavior of the chemically bonded Ni, offers an excellent proton reduction process as shown in Figure 10B. Upon the irradiation, the excited electrons are trapped (as shown in eqs 2 and 3), and they first lead to the formation of an intermediate HNi-S by absorption-reduction of H^+ and then generate H_2 by the subsequent reduction of H^+ as shown in eqs 4 and 5.[48−50] The possibility of the formation of such type of HNi-S intermediate has been demonstrated through computational and experimental studies of hydro-treating processes.[51]

$$\text{S:g} - C_3N_4 + h\nu \rightarrow e^-(\text{CB, S:g} - C_3N_4) + h^+(\text{VB, S:g} - C_3N_4) \quad (2)$$

$$\text{Ni} + e^-(\text{CB, S:g} - C_3N_4) \rightarrow e^-(\text{Ni}) + \text{S:g} - C_3N_4 \quad (3)$$

$$\text{Ni} - \text{S} + e^- + H^+ \leftrightarrow \text{HNi} - \text{S} \quad (4)$$

$$\text{HNi} - \text{S} + e^- + H^+ \leftrightarrow H_2 + \text{Ni} - \text{S} \quad (5)$$

Apart from these chemical-structures induced contributions, the observed features in the physical structures such as the reduced size and nanoholes (pores) on the surface of Ni-SCN also facilitated a stronger interaction between the catalyst and surrounding molecules, which could also be attributed to the observed enhanced photocatalytic H_2 generation efficiency of the chemically bonded Ni-SCN system.

CONCLUSION

In summary, nickel supported S-doped g-C_3N_4 (Ni-SCN) nanosheets were successfully prepared through calcination of dicyanamide followed by sulfidation process. The obtained hydrogen production efficiency of Ni-SCN was found to be around 72.5, 10.5, and 1.5 folds higher than that of the bare SCN, Ni-GCN, and Pt-SCN, respectively. The apparent quantum yield was found to be 17.2% at 420 nm. The observed enhanced photocatalytic activity of Ni-SCN was attributed to the extended visible light absorption, high surface area, and the synergistic effect between the host SCN photocatalyst and the chemically bonded nickel cocatalyst through Ni−S−C-N chemical bonds, which enhanced the rapid charge separation and transportation and self-catalytic behavior of the Ni cocatalyst. From the obtained results, the chemical bonding of cocatalyst onto the photocatalyst can be realized as a promising strategy as compared to the other conventional deposition strategies, which eventually has the potential to replace the deposition of noble-metals as cocatalyst toward enhancing the visible light driven photocatalytic hydrogen production.

ASSOCIATED CONTENT

Supporting Information

The Supporting Information is available free of charge on the ACS Publications website at DOI: 10.1021/acssuschemeng.7b04598.

Literature comparison of the obtained efficiency of the material (Table S1), results of elemental analysis (Table S2 and Table S3), photographic images of the samples (Figure S1(a)-(b)), photocatalytic hydrogen production of the samples (Figure S2(a)-(b)), TEM image and XPS spectrum of the recycled sample (Figure S3(a)-(b). (PDF)

AUTHOR INFORMATION

Corresponding Author

*E-mail: trong-on.do@gch.ulaval.ca.

ORCID

Trong-On Do: 0000-0002-7785-5299

Notes

The authors declare no competing financial interest.

ACKNOWLEDGMENTS

This work was supported by the Natural Science and Engineering Research Council of Canada (NSERC) through the Collaborative Research and Development (CRD), Strategic Project (SP), and Discovery Grants. The authors would like to thank EXP Inc. and SiliCycle Inc. for their support.

REFERENCES

(1) Dresselhaus, M. S.; Thomas, I. L. Alternative energy technologies. *Nature* **2001**, *414*, 332.

(2) Su, C.-Y.; Cheng, H.; Li, W.; Liu, Z.-Q.; Li, N.; Hou, Z.; Bai, F.-Q.; Zhang, H.-X.; Ma, T.-Y. Zinc-Air Batteries: Atomic Modulation of FeCo−Nitrogen−Carbon Bifunctional Oxygen Electrodes for Rechargeable and Flexible All-Solid-State Zinc−Air Battery (Adv. Energy Mater. 13/2017). *Adv. Energy Mater.* **2017**, *7* (13), 70067.

(3) Liu, Z.-Q.; Cheng, H.; Li, N.; Ma, T. Y.; Su, Y.-Z. ZnCo2O4 Quantum Dots Anchored on Nitrogen-Doped Carbon Nanotubes as Reversible Oxygen Reduction/Evolution Electrocatalysts. *Adv. Mater.* **2016**, *28* (19), 3777−3784.

(4) Cao, S.; Low, J.; Yu, J.; Jaroniec, M. Polymeric Photocatalysts Based on Graphitic Carbon Nitride. *Adv. Mater.* **2015**, *27* (13), 2150−2176.

(5) Wei, R.-B.; Kuang, P.-Y.; Cheng, H.; Chen, Y.-B.; Long, J.-Y.; Zhang, M.-Y.; Liu, Z.-Q. Plasmon-Enhanced Photoelectrochemical Water Splitting on Gold Nanoparticle Decorated ZnO/CdS Nanotube Arrays. *ACS Sustainable Chem. Eng.* **2017**, *5* (5), 4249−4257.

(6) Zhu, M.; Zhai, C.; Sun, M.; Hu, Y.; Yan, B.; Du, Y. Ultrathin graphitic C_3N_4 nanosheet as a promising visible-light-activated support for boosting photoelectrocatalytic methanol oxidation. *Appl. Catal., B* **2017**, *203*, 108−115.

(7) Bi, L.; Meng, D.; Bu, Q.; Lin, Y.; Wang, D.; Xie, T. Electron acceptor of Ni decorated porous carbon nitride applied in photocatalytic hydrogen production. *Phys. Chem. Chem. Phys.* **2016**, *18* (46), 31534−31541.

(8) Wang, X.; Maeda, K.; Thomas, A.; Takanabe, K.; Xin, G.; Carlsson, J. M.; Domen, K.; Antonietti, M. A metal-free polymeric photocatalyst for hydrogen production from water under visible light. *Nat. Mater.* **2009**, *8* (1), 76−80.

(9) Zheng, D.; Pang, C.; Liu, Y.; Wang, X. Shell-engineering of hollow g-C_3N_4 nanospheres via copolymerization for photocatalytic hydrogen evolution. *Chem. Commun.* **2015**, *51* (47), 9706−9709.

(10) Liang, Q.; Li, Z.; Yu, X.; Huang, Z.-H.; Kang, F.; Yang, Q.-H. Macroscopic 3D Porous Graphitic Carbon Nitride Monolith for Enhanced Photocatalytic Hydrogen Evolution. *Adv. Mater.* **2015**, *27* (31), 4634−4639.

(11) Kailasam, K.; Epping, J. D.; Thomas, A.; Losse, S.; Junge, H. Mesoporous carbon nitride-silica composites by a combined sol-gel/thermal condensation approach and their application as photocatalysts. *Energy Environ. Sci.* **2011**, *4* (11), 4668−4674.

(12) Schwinghammer, K.; Tuffy, B.; Mesch, M. B.; Wirnhier, E.; Martineau, C.; Taulelle, F.; Schnick, W.; Senker, J.; Lotsch, B. V. Triazine-based Carbon Nitrides for Visible-Light-Driven Hydrogen Evolution. *Angew. Chem., Int. Ed.* **2013**, *52* (9), 2435−2439.

(13) Xiong, T.; Cen, W.; Zhang, Y.; Dong, F. Bridging the g-C_3N_4 Interlayers for Enhanced Photocatalysis. *ACS Catal.* **2016**, *6* (4), 2462−2472.
(14) Gao, D.; Liu, Y.; Liu, P.; Si, M.; Xue, D. Atomically Thin B doped g-C_3N_4 Nanosheets: High-Temperature Ferromagnetism and calculated Half-Metallicity. *Sci. Rep.* **2016**, *6*, 35768.
(15) Wang, K.; Li, Q.; Liu, B.; Cheng, B.; Ho, W.; Yu, J. Sulfur-doped g-C_3N_4 with enhanced photocatalytic CO2-reduction performance. *Appl. Catal., B* **2015**, *176*, 44−52.
(16) Zhou, Y.; Zhang, L.; Liu, J.; Fan, X.; Wang, B.; Wang, M.; Ren, W.; Wang, J.; Li, M.; Shi, J. Brand new P-doped g-C3N4: enhanced photocatalytic activity for H2 evolution and Rhodamine B degradation under visible light. *J. Mater. Chem. A* **2015**, *3* (7), 3862−3867.
(17) Reli, M.; Huo, P.; Šihor, M.; Ambrožová, N.; Troppová, I.; Matějová, L.; Lang, J.; Svoboda, L.; Kuśtrowski, P.; Ritz, M.; Praus, P.; Kočí, K. Novel TiO_2/C_3N_4 Photocatalysts for Photocatalytic Reduction of CO_2 and for Photocatalytic Decomposition of N_2O. *J. Phys. Chem. A* **2016**, *120* (43), 8564−8573.
(18) Li, D.; Shi, F.; Jiang, D.; Chen, M.; Shi, W. $CdIn_2S_4$/g-C_3N_4 heterojunction photocatalysts: enhanced photocatalytic performance and charge transfer mechanism. *RSC Adv.* **2017**, *7* (1), 231−237.
(19) Xu, Y.; Fu, Z.-C.; Cao, S.; Chen, Y.; Fu, W.-F. Highly selective oxidation of sulfides on a CdS/C3N4 catalyst with dioxygen under visible-light irradiation. *Catal. Sci. Technol.* **2017**, *7* (3), 587−595.
(20) Naseri, A.; Samadi, M.; Pourjavadi, A.; Moshfegh, A. Z.; Ramakrishna, S. Graphitic carbon nitride (g-C3N4)-based photocatalysts for solar hydrogen generation: recent advances and future development directions. *J. Mater. Chem. A* **2017**, *5* (45), 23406−23433.
(21) Niu, P.; Zhang, L.; Liu, G.; Cheng, H.-M. Graphene-Like Carbon Nitride Nanosheets for Improved Photocatalytic Activities. *Adv. Funct. Mater.* **2012**, *22* (22), 4763−4770.
(22) Wang, N.; Fan, H.; Sun, J.; Han, Z.; Dong, J.; Ai, S. Fluorine-doped carbon nitride quantum dots: Ethylene glycol-assisted synthesis, fluorescent properties, and their application for bacterial imaging. *Carbon* **2016**, *109*, 141−148.
(23) Shao, X.; Xu, J.; Huang, Y.; Su, X.; Duan, H.; Wang, X.; Zhang, T. Pd@C_3N_4 nanocatalyst for highly efficient hydrogen storage system based on potassium bicarbonate/formate. *AIChE J.* **2016**, *62* (7), 2410−2418.
(24) Liang, S.; Xia, Y.; Zhu, S.; Zheng, S.; He, Y.; Bi, J.; Liu, M.; Wu, L. Au and Pt co-loaded g-C_3N_4 nanosheets for enhanced photocatalytic hydrogen production under visible light irradiation. *Appl. Surf. Sci.* **2015**, *358*, 304−312.
(25) Liu, G.; Niu, P.; Sun, C.; Smith, S. C.; Chen, Z.; Lu, G. Q.; Cheng, H.-M. Unique Electronic Structure Induced High Photoreactivity of Sulfur-Doped Graphitic C_3N_4. *J. Am. Chem. Soc.* **2010**, *132* (33), 11642−11648.
(26) Samadi, M.; Zirak, M.; Naseri, A.; Khorashadizade, E.; Moshfegh, A. Z. Recent progress on doped ZnO nanostructures for visible-light photocatalysis. *Thin Solid Films* **2016**, *605*, 2−19.
(27) Liu, G.; Wang, L.; Yang, H. G.; Cheng, H.-M.; Lu, G. Q. Titania-based photocatalysts-crystal growth, doping and heterostructuring. *J. Mater. Chem.* **2010**, *20* (5), 831−843.
(28) Ma, X.; Lv, Y.; Xu, J.; Liu, Y.; Zhang, R.; Zhu, Y. A Strategy of Enhancing the Photoactivity of g-C3N4 via Doping of Nonmetal Elements: A First-Principles Study. *J. Phys. Chem. C* **2012**, *116* (44), 23485−23493.
(29) Lu, Y.; Chu, D.; Zhu, M.; Du, Y.; Yang, P. Exfoliated carbon nitride nanosheets decorated with NiS as an efficient noble-metal-free visible-light-driven photocatalyst for hydrogen evolution. *Phys. Chem. Chem. Phys.* **2015**, *17* (26), 17355−17361.
(30) Chen, G.-F.; Ma, T. Y.; Liu, Z.-Q.; Li, N.; Su, Y.-Z.; Davey, K.; Qiao, S.-Z. Efficient and Stable Bifunctional Electrocatalysts Ni/NixMy (M = P, S) for Overall Water Splitting. *Adv. Funct. Mater.* **2016**, *26* (19), 3314−3323.
(31) Wang, Y.; Wu, J.; Zheng, J.; Jiang, R.; Xu, R. Ni^{2+}-doped $Zn_xCd_{1-x}S$ photocatalysts from single-source precursors for efficient solar hydrogen production under visible light irradiation. *Catal. Sci. Technol.* **2012**, *2* (3), 581−588.
(32) Liu, M.; Chen, Y.; Su, J.; Shi, J.; Wang, X.; Guo, L. Photocatalytic hydrogen production using twinned nanocrystals and an unanchored NiSx co-catalyst. *Nat. Energy* **2016**, *1*, 16151.
(33) Simon, T.; Bouchonville, N.; Berr, M. J.; Vaneski, A.; Adrović, A.; Volbers, D.; Wyrwich, R.; Döblinger, M.; Susha, A. S.; Rogach, A. L.; Jäckel, F.; Stolarczyk, J. K.; Feldmann, J. Redox shuttle mechanism enhances photocatalytic H_2 generation on Ni-decorated CdS nanorods. *Nat. Mater.* **2014**, *13* (11), 1013−1018.
(34) Li, S.; Dai, D.; Ge, L.; Gao, Y.; Han, C.; Xiao, N. Synthesis of layer-like $Ni(OH)_2$ decorated $ZnIn_2S_4$ sub-microspheres with enhanced visible-light photocatalytic hydrogen production activity. *Dalton Transactions* **2017**, *46*, 10620.
(35) Indra, A.; Menezes, P. W.; Kailasam, K.; Hollmann, D.; Schroder, M.; Thomas, A.; Bruckner, A.; Driess, M. Nickel as a co-catalyst for photocatalytic hydrogen evolution on graphitic-carbon nitride (sg-CN): what is the nature of the active species? *Chem. Commun.* **2016**, *52* (1), 104−107.
(36) Chen, Z.; Sun, P.; Fan, B.; Zhang, Z.; Fang, X. In Situ Template-Free Ion-Exchange Process to Prepare Visible-Light-Active g-C_3N_4/NiS Hybrid Photocatalysts with Enhanced Hydrogen Evolution Activity. *J. Phys. Chem. C* **2014**, *118* (15), 7801−7807.
(37) Liang, Q.; Li, Z.; Huang, Z.-H.; Kang, F.; Yang, Q.-H. Holey Graphitic Carbon Nitride Nanosheets with Carbon Vacancies for Highly Improved Photocatalytic Hydrogen Production. *Adv. Funct. Mater.* **2015**, *25* (44), 6885−6892.
(38) Xu, C.; Han, Q.; Zhao, Y.; Wang, L.; Li, Y.; Qu, L. Sulfur-doped graphitic carbon nitride decorated with graphene quantum dots for an efficient metal-free electrocatalyst. *J. Mater. Chem. A* **2015**, *3* (5), 1841−1846.
(39) Stolbov, S.; Zuluaga, S. Sulfur doping effects on the electronic and geometric structures of graphitic carbon nitride photocatalyst: insights from first principles. *J. Phys.: Condens. Matter* **2013**, *25* (8), 085507.
(40) Sun, L.; Yang, M.; Huang, J.; Yu, D.; Hong, W.; Chen, X. Freestanding Graphitic Carbon Nitride Photonic Crystals for Enhanced Photocatalysis. *Adv. Funct. Mater.* **2016**, *26* (27), 4943−4950.
(41) Zhang, X.; Gong, Y.; Dong, X.; Zhang, X.; Ma, C.; Shi, F. Fabrication and efficient visible light-induced photocatalytic activity of $Bi_2WO_6/BiVO_4$ heterojunction. *Mater. Chem. Phys.* **2012**, *136* (2), 472−476.
(42) Zhang, X.; Du, L.; Wang, H.; Dong, X.; Zhang, X.; Ma, C.; Ma, H. Highly ordered mesoporous BiVO4: Controllable ordering degree and super photocatalytic ability under visible light. *Microporous Mesoporous Mater.* **2013**, *173*, 175−180.
(43) Yu, J.; Wang, K.; Xiao, W.; Cheng, B. Photocatalytic reduction of CO_2 into hydrocarbon solar fuels over g-C_3N_4-Pt nanocomposite photocatalysts. *Phys. Chem. Chem. Phys.* **2014**, *16* (23), 11492−11501.
(44) Liao, G.; Chen, S.; Quan, X.; Yu, H.; Zhao, H. Graphene oxide modified g-C_3N_4 hybrid with enhanced photocatalytic capability under visible light irradiation. *J. Mater. Chem.* **2012**, *22* (6), 2721−2726.
(45) Yu, J.; Wang, S.; Cheng, B.; Lin, Z.; Huang, F. Noble metal-free $Ni(OH)_2$-g-C_3N_4 composite photocatalyst with enhanced visible-light photocatalytic H2-production activity. *Catal. Sci. Technol.* **2013**, *3* (7), 1782−1789.
(46) Yang, Y.; Guo, Y.; Liu, F.; Yuan, X.; Guo, Y.; Zhang, S.; Guo, W.; Huo, M. Preparation and enhanced visible-light photocatalytic activity of silver deposited graphitic carbon nitride plasmonic photocatalyst. *Appl. Catal., B* **2013**, *142*, 828−837.
(47) Bai, X.; Wang, L.; Zong, R.; Zhu, Y. Photocatalytic Activity Enhanced via g-C_3N_4 Nanoplates to Nanorods. *J. Phys. Chem. C* **2013**, *117* (19), 9952−9961.
(48) Zhang, W.; Wang, Y.; Wang, Z.; Zhong, Z.; Xu, R. Highly efficient and noble metal-free NiS/CdS photocatalysts for H_2 evolution from lactic acid sacrificial solution under visible light. *Chem. Commun.* **2010**, *46* (40), 7631−7633.

DOI: 10.1021/acssuschemeng.7b04598
ACS Sustainable Chem. Eng. 2018, 6, 4194−4203

(49) Li, Y.; Lin, S.; Peng, S.; Lu, G.; Li, S. Modification of ZnS1−x−0.5yOx(OH)y−ZnO photocatalyst with NiS for enhanced visible-light-driven hydrogen generation from seawater. *Int. J. Hydrogen Energy* **2013**, *38* (36), 15976−15984.
(50) Zhang, L.; Tian, B.; Chen, F.; Zhang, J. Nickel sulfide as co-catalyst on nanostructured TiO_2 for photocatalytic hydrogen evolution. *Int. J. Hydrogen Energy* **2012**, *37* (22), 17060−17067.
(51) Breysse, M.; Furimsky, E.; Kasztelan, S.; Lacroix, M.; Perot, G. Hydrogen activation by transition metal sulfides. *Catal. Rev.: Sci. Eng.* **2002**, *44* (4), 651−735.

DOI: 10.1021/acssuschemeng.7b04598
ACS Sustainable Chem. Eng. 2018, 6, 4194−4203